SCIENTIFIC REPORTS

OPEN

SUBJECT AREAS:
TRANSLATIONAL RESEARCH
DRUG DELIVERY
BIOMEDICAL MATERIALS
TISSUE ENGINEERING

Received
12 June 2013

Accepted
23 August 2013

Published
13 September 2013

Correspondence and requests for materials should be addressed to N.G. (guning@seu.edu.cn) or H.X. (xuhy@pumc.edu.cn)

* These authors contributed equally to this work.

Super-paramagnetic responsive nanofibrous scaffolds under static magnetic field enhance osteogenesis for bone repair *in vivo*

Jie Meng[1]*, Bo Xiao[2]*, Yu Zhang[3], Jian Liu[1], Huadan Xue[4], Jing Lei[1], Hua Kong[1], Yuguang Huang[2], Zhengyu Jin[4], Ning Gu[3] & Haiyan Xu[1]

[1]Department of Biomedical Engineering, Institute of Basic Medical Sciences, Chinese Academy of Medical Science & Peking Union Medical College, [2]Department of Anesthesiology, Peking Union Medical College Hospital, Chinese Academy of Medical Science & Peking Union Medical College, [3]School of Biological Science and Medical Engineering, Southeastern University, [4]Department of Radiology, Peking Union Medical College Hospital, Chinese Academy of Medical Science & Peking Union Medical College.

A novel nanofibrous composite scaffold composed of super-paramagnetic γ-Fe_2O_3 nanoparticles (MNP), hydroxyapatite nanoparticles (nHA) and poly lactide acid (PLA) was prepared using electrospinning technique. The scaffold well responds extern static magnetic field with typical saturation magnetization value of 0.049 emu/g as well as possesses nanofibrous architecture. The scaffolds were implanted in white rabbit model of lumbar transverse defects. Permanent magnets are fixed in the rabbit cages to provide static magnetic field for the rabbits post surgery. Results show that MNP incorporated in the nanofibers endows the scaffolds super-paramagnetic responsive under the applied static magnetic field, which accelerates new bone tissue formation and remodeling in the rabbit defect. The scaffold also exhibits good compatibility of CK, Cr, ALT and ALP within normal limits in the serum within 110 days post implantation. In conclusion, the super-paramagnetic responding scaffold with applying of external magnetic field provides a novel strategy for scaffold-guided bone repair.

Bone repair by scaffold-guiding regeneration is widely demanded in critical size bone defects resulted from trauma, tumor, resection and skeletal abnormalities. Successful regeneration largely depends on interface interactions between bone related cells and scaffolds. Although varieties of scaffolds for bone regeneration have been investigated as alternatives to autologous or allogeneic bone grafts[1–5], there is still large space for improvement to meet clinical requirements.

Osteoblast cell is one kind of bone related effector cells, and in particular, they are mechanical sensitive. It has been accepted that bone tissue responds to mechanical stimulation with bone formation and inhibition of bone resorption[6]. Therefore, proper physical stimulation can play positive roles in osteogenesis. Some mechanical stimulators such as stress, strain, strain energy, and strain rate have been demonstrated enhancement to bone regeneration and fracture healing[7–11].

Besides mechanical force stimuli above mentioned, magnetic stimulation originated from static or alternative magnetic fields has constantly attracted researchers' interests as well. For instances, several groups reported that weak magnetic or pulse electromagnetic fields of Gauss order are one effective stimuli that promoted bone fracture healing, spinal fusion, bone ingrowths into ceramics in animal models[12–20]. Strong static magnetic field of 5–10 T was also reported to have the potency of regulating the orientation of matrix proteins and cells *in vitro* and *in vivo*[21–32].

Regarding to the beneficial effects of magnetic fields on bone fracture healing and new bone formation, we consider introducing magnetic stimulation into nanofibrous scaffolds that have been widely used for bone tissue repair. Iron oxide nanoparticles show a super-paramagnetic behavior[33], this property is still preserved as nanocomposite materials based on a polyester matrix incorporating iron oxide nanoparticles are considered[34]. We previously reported that a nanofibrous composite composed of super-paramagnetic iron oxide nanoparticles (MNP), hydroxyapatite nanoparticles (nHA) and poly lactide acid (PLA) produces super-paramagnetic responses under an applied static magnetic field and accelerates proliferation and differentiation of osteoblast cells *in vitro* in reference to the nanofibrous scaffold without MNP under the same magnetic field[35]. In the nanofibrous composite, MNP is used to give super-paramagnetic response, nHA is for bone conductivity and PLA for nanofibers fabrication. Other researchers also reported that porous hydroxyapatite scaffolds containing magnetic nanoparticles enhance the osteoblast cells growth *in vitro* when a magnetic field is applied to the cell culture system[36,37]. Another composite composed of a polyester matrix magnetically functionalized with iron oxide nanoparticles shows a good ability to support and enhance osteogenic differentiate of mesenchimal stem cells[38]. Nevertheless, *in vivo* study for the new bone-formation enhancement mediated by magnetic or super-paramagnetic responsive composites has been rarely reported, that is necessary and crucial for clinical applications of the composites.

The aim of this work is to validate *in vivo* osteogenesis enhancement of the super-paramagnetic nanofibrous scaffold synergizing with external static magnetic field. The scaffolds were implanted in the lumbar transverse defect of New Zealand white rabbits. External static magnetic field was applied by fixing permanent magnets to the rabbit cages of opposite sides. The osteogenesis effect of the scaffold synergizing with the statistic field was investigated within 110 days post implantation surgery by CT scan analysis, micro-CT analysis and pathological observations. We show that the super-paramagnetic nanofibrous scaffold accelerates bone tissue regeneration in situ under the external magnetic field and eventually led to faster repair of bone defect in reference to that without external magnetic field. This effect is attributed to the magnetic stimulation originated from the response of MNP embedded in the nanofibers to the external magnetic field.

Results

Super-paramagnetic responsive performance and microstructure of the composite scaffold. The original composite was a brown nonwoven film obtained from the mixture of poly lactide acid (PLA), hydroxyapatite nanoparticles (nHA) and super-paramagnetic γ-Fe_2O_3 nanoparticles (MNP) in DMAc using electrospinning technique. Each film was carefully folded and fixed to pellets with the same volume and mass (Figure 1a), and then were implanted in situ of the bone defect as shown in the schematic graph (Figure 1b). The scaffold had nanofibrous network under scanning electron microscopy (SEM). Diameter of the fibers ranged from 300 nm to 1000 nm. The average value of the diameters was 805 ± 113 nm, which was calculated from statistically counting and measuring more than 100 fibers randomly taken in ten of SEM images. Depositing layer by layer on the metal collector in the electrospinning, the fibers in the film entangled randomly and formed connecting network structure. The pores formed by entangled fibers were mostly in micrometer scale, majority of the pore size under SEM is about 10 ~ 20 μm (Figure 1c). The MNP (dark black shadows under TEM due to their high electron density) mainly located inside the fibers, while nHA (gray shadows due to their low electron density under TEM) mainly distributed near the surface of the fibers (Figure 1d). We previously reported that fibres composed of MNP and PLA have a smooth surface, while the surface of the fibres of either MNP/nHA/PLA or nHA/PLA was rough with particulates that are considered attribution of nHA that was embedded in the composite fibres[35]. The TEM observation provides further distribution information of the two kinds of nanoparticles and suggests the particulates near to the fibres surface under SEM are nHA. Those embedded nHA are benefit in improving bone compatibility of PLA. The nanofibrous composite films could produce super-paramagnetic response well with typical saturation magnetization value of 0.049 emu/g, which was same with that reported previously[35] and attributable to MNP incorporation[39].

Pathological observations. The tissue containing filled defects were taken out on day 10, 20 and 30 post the implantation and conducted conventional HE and perl's staining. Figure 2 presented representative photographs at different time points. Under light microscope, the scaffold was brown in the samples of H&E staining. It could be seen that the implanted scaffolds surrounded by different cells on day 10, mainly including macrophages (circled by green line and pointed by green arrow) and fibroblasts (pointed by yellow arrow). This indicates that the scaffolds recruite host-derived cells migrating to the defects area. The macrophages engulfed scaffold materials and became brown. Macrophage influx and fibroblasts surrounding are typical reactions of the host responding to foreign implants. At this time point, vessel structures with feature of endothelium cells arranging in circle appeared (pointed by blue arrow), and they were occasionally observed around the scaffolds. On day 20, the implanted scaffolds were separated into smaller pieces by the cells and the total brown area was reduced, suggesting that the scaffolds are degraded and absorbed over time. Along with above changes, osteoblast cells (pointed by red arrow) appeared and pink area around the scaffolds increased, indicating that bone repair process is initiated and new bone tissue formed around the scaffold pieces, because extracellular matrix substance is mainly composed of collagen appearing pink color by H&E staining. Meanwhile more vessel structures were seen very near around the scaffold pieces, implying that oxygen and nutrients can be supplied to support proliferation and differentiation of the osteoblast cells. On day 30, less scaffold pieces and more new bone tissue were observed, while macrophages and fibroblasts disappeared. In order to show the scaffolds degradation more clearly, perl's staining was used to make the scaffolds appear blue due to iron content. Results show that original blue area was separated into smaller pieces and the total blue area was reduced over time, giving further evidence that the scaffold is degraded and absorbed over time.

It is noticeable that during above process, both degradation rate and new bone formation for group S + M are faster than those for group S at each time point, which is attributable to the stimulation resulting from super-paramagnetic response due to MNP incorporation in the nanofibers. To make further confirmation, immunohistochemical staining was applied to detect the level of osteocalcin (OC) which is one bone-specific extracellular matrix protein produced by the osteoblast cells in new bone formation. At each testing time point, Group S + M exhibited higher level of OC than group S (Figure 3), showing more red-brown area (surrounded by red line). Particularly, group S + M showed the highest level of OC on the day 20 post surgery, suggesting that the scaffold induces the highest activity of

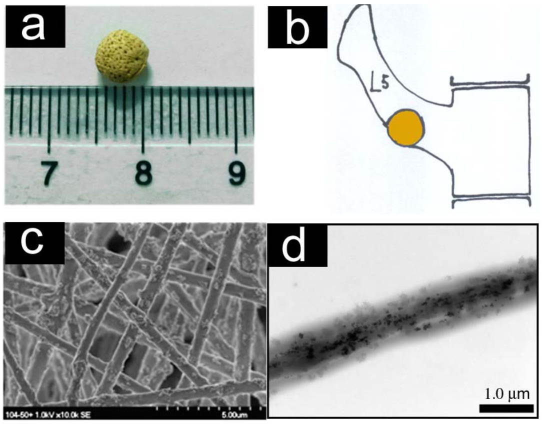

Figure 1 | Characterization of the super-paramagnetic nanofibrous scaffolds. (a): The scaffold pellet with diameter of ~ 5 mm. (b): Scheme image of the scaffold pellet being implanted in the defect of transverse process of L5 of rabbits. (c): SEM image of the scaffold showing randomly tangled nanofibers with diameter ranging from 300 nm to 1000 nm. (d): TEM image of fibers in the scaffold.

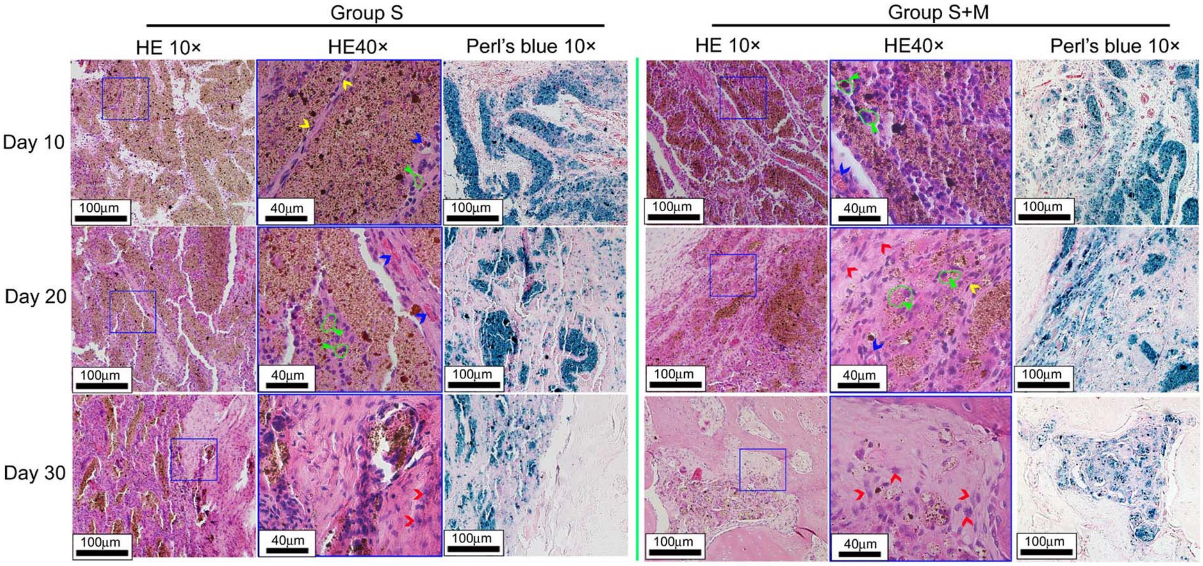

Figure 2 | Representative histological images of the scaffolds implanted in the bone defect on day 10, 20, 30 post implantation. Left column: Groups S; Right column: Group S + M. Macrophages were circled by green line and pointed by green arrow; Fibroblasts were pointed by yellow arrow; Vessels were pointed by blue arrow; Osteoblast cells were pointed by red arrow.

new ECM secretion at that time point in synergizing with the applied magnetic field. At the same time, the implanted scaffolds became smaller (labeled by green rhombus).

Sirus red stain was also employed to examine collagen deposition in the new extracellular matrix development. As shown in Figure 4, at each time point, group S + M exhibited more collagen content that group S, in particular, it exhibited clearer and denser collagen fibers on the day 30 in reference to group S. These are consistent with the observations of H&E, indicating that there are more osteoblast cells in higher activity on day 20, leading to more new bone tissue formation on day 30.

Radiological observations. Additional to the pathological observation, radiological analysis of CT scan was conducted with the rabbits at different time points after the surgery (Figure 5). CT images showed incomplete fracture in the right transverse process either in group S or group S + M on day 10 after implantation. The scaffold showed lower density in the defect compared with the natural bone in the CT scan. On the day 10, the filled defect exhibited not homogeneous with blurred bright spots. The density of the area became stronger and homogeneous over time. On the day 50, the cortical bone had become connected and homogeneous, and the bone marrow cavity was mostly clear for group S + M, suggesting the new bone tissue has formed clear and organized morphology; instead, there was still non-homogeneous bone density hyperplasia for group S. These indicate that the applied static magnetic field promotes density increase of the defects area. On the day 90, bony connection was further improved in both groups. The shape of newly formed bone in group S + M became further homogenous, and the shape was very similar to that of natural bone, while the one in group S still showed thick and not continuous. These suggest that group S + M has completed the repair process, which is faster than group S. The

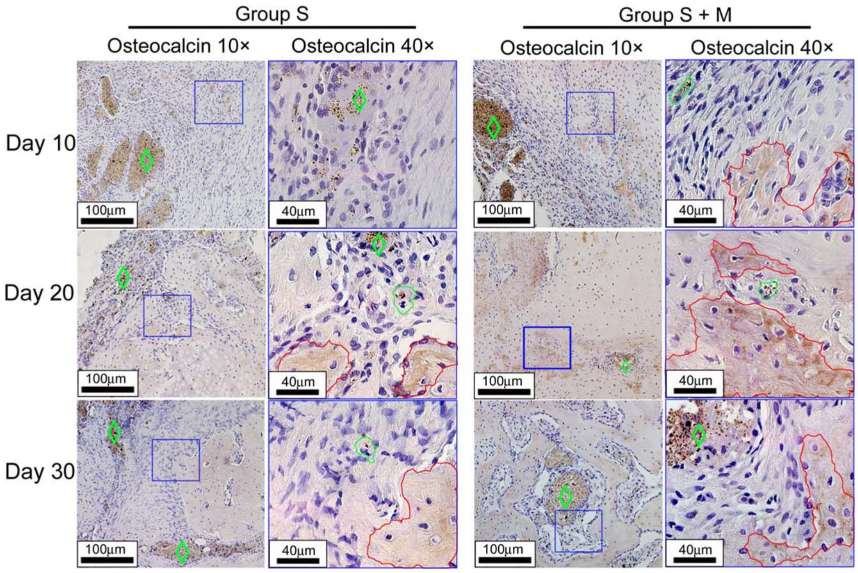

Figure 3 | Osteocalcin (OC) expression induced by the scaffolds implanted in the bone defect on day 10, 20, and 30 post implantation. Left column: Groups S; Right column: Group S + M. OC positive cells were circled by red line; the scaffolds were labeled by green rhombus.

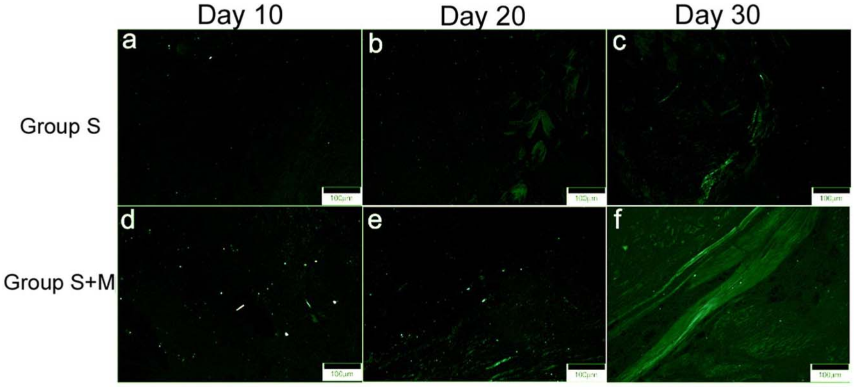

Figure 4 | **Sirius red stain for the collagen deposition in the scaffolds implanted in the bone defect on day 10, 20, and 30 post implantation.**

imaging findings are consistent with corresponding pathological results.

Micro-CT measurement. Bone remodeling is one crucial step in the late of defect repair, in which the newly formed bone tissue will be reshaping by osteoclast cells, thus the newly formed bone tissue can match the shape and size of natural bone well. We next conducted micro-CT with the tissues excised from the repaired defects in situ on the day 110 to examine and compare the newly formed bone amount in the different groups. Figure 6A gave a comparison of the bone amount in the repaired defects. The bone amount for group S + M was lower than that for group S, suggesting that the remodeling process for group S + M is faster than that for group S. Pathological observation on day 110 after implantation supports the results of micro-CT. The implanted scaffold was completely absorbed for group S + M (Figure 6c), while there were small amount of scaffold remained for group S (Figure 6b). Additionally, the newly formed bone tissue was homogenous and well organized for group S + M, while the bone tissue for group S was thicker than that for group S + M. The result provides further evidence that group S + M completes the bone remodeling faster than group S.

Evaluation of biocompatibility. All 24 rabbits survived the planned duration of the experiment. The rabbits revived within 2 h after the operation and could stand well and move freely in 24 h. The surgical lesions of all animals healed well without clinical signs of inflammation. All the animals gained weight in the post-operative period. Visual inspection after removal of bone defect showed seemingly well integrated scaffolds in the healed cortical bone.

After euthanasia, the kidney, lung, liver, heart, spleen from all the animals were evaluated for potential abnormalities such as organ swelling, hemorrhage. The organs were further underwent conventional H&E staining. There are no indications of any pathological changes caused by the experiment (data not shown). The scaffold's biocompatibility was also evaluated by determining biochemical parameters of creatinine (CR) and creatinine kinase (CK) for kidney function, alanine aminatransferase (ALT) and alkaline phosphatase (ALP) for liver function. Figure 7 gave a summary of biochemistry analysis for the blood samples collected on day 30 post the implantation from the different group. The detected items were within the normal limits. Taken together, the scaffold did not exhibit any harmful signs in the biocompatibility.

Discussion

Electrospun nanofibrous scaffold can provide a suitable environment for cell attachment and growth by mimicking the structure of natural extracellular matrices (ECMs)[40–44]. Here we incorporated MNP in the nanofibers, expecting to give the fibers novel function of responding the applied magnetic field. The advantage of incorporation MNP in the scaffold is that MNP became an intrinsic component of the scaffold, which allows them produce huge amounts of miniature magnetic force in the scaffold under the external magnetic field to continually stimulate osteoblast cells proliferation and secretion of new ECM. Louis Yuge et al. reported that in conventional cells culture system, weak magnetic force with intensity of 10–50 mT accelerated osteoblast differentiation and this effect was largely attributed to the increased phosphorylation of p38[45]. At the same time, the nanofibrous structure of the scaffold provides to mimic microenvironment of natural extra cellular matrix. As expected, the scaffold under the external magnetic field induced earlier and higher amount of osteocalcin positive cells in situ, leading to the earlier and faster bone formation in the defect, evidenced by the faster achievement of cortical bone and medullar cavity continuity as well as by the pathological observations, when compared with that without magnetic fields. These strongly suggest continuous weak magnetic force stimulation have significant effect on the bone regeneration and repair, and the effect can be realized by applying an external magnetic field to super-paramagnetic responsive scaffolds.

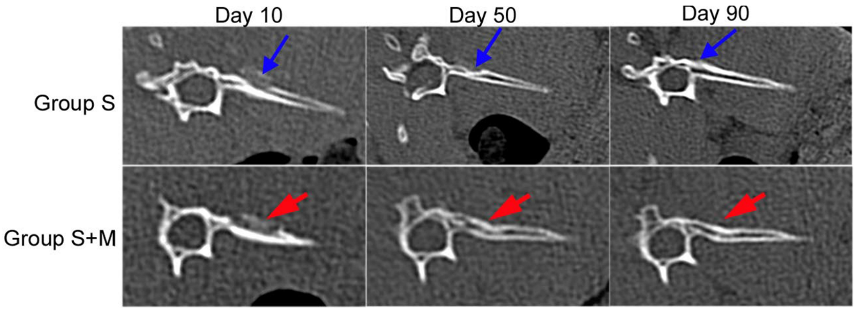

Figure 5 | **CT images of the bone defects for group S and Group S + M post 10, 50 and 90 days implantation.** The arrows pointed to the defects.

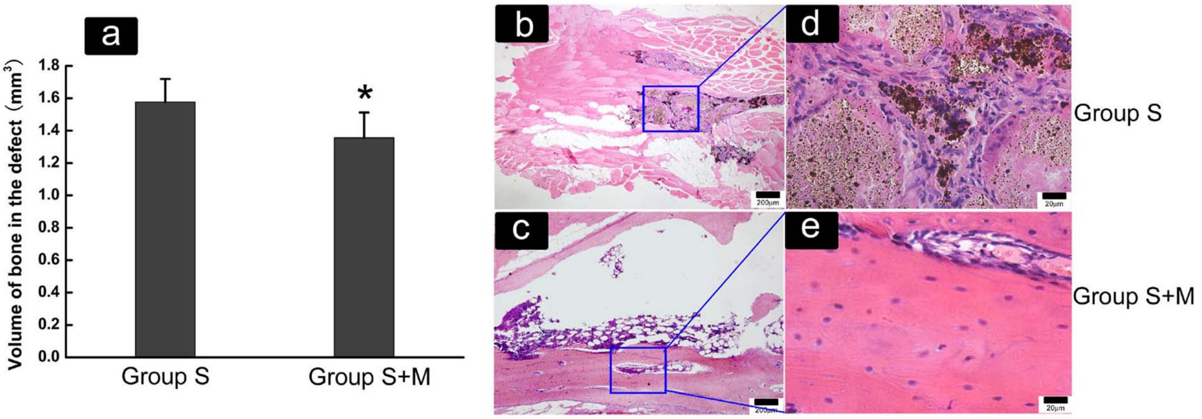

Figure 6 | **New bone formation analyzed by Micro-CT and histological observation on 110 day post implantation.** (a): The amount of the new bone formed in the defects obtained from Micro-CT. (b) and (c): Histological observation of the bone defects in group S and group S + M respectively. (d): Magnification of b, showing small amount of the scaffolds remaining unabsorbed after 110 days implantation. (e): Magnification of c, showing a homogenous and well organized bone formation in the defect.

Besides new bone tissue formation, degradation rate for the scaffold is another important factor that determines bone repair. Too slow degradation of scaffold may hinder the formation and maturation of new bones at the late stage of bone healing. Under the external magnetic field, the scaffold degrades faster than that without the external magnetic field. It is likely that macrophages recruited by the scaffold are more active due to the magnetic stimulation from the scaffold under the external magnetic field. The enhancement effect of the scaffold on osteogenesis is encouraging. Underlying mechanisms and the relationship between macrophages, magnetic field and scaffold degradation are worth further exploitations, which is benefit in optimizing magnetic strength and modulating better osteogenesis effects in the future.

In conclusion, the novel super-paramagnetic nanofibrous composite scaffold accelerated new bone tissue formation and remodeling through synergizing with the applied static magnetic field, which provides a promising new strategy of guiding and enhancing bone repair in situ.

Methods

Preparation and characterization of super-paramagnetic nanofibrous scaffold. Super-paramagnetic nanoparticles of γ-Fe_2O_3 coated with meso-2, 3-

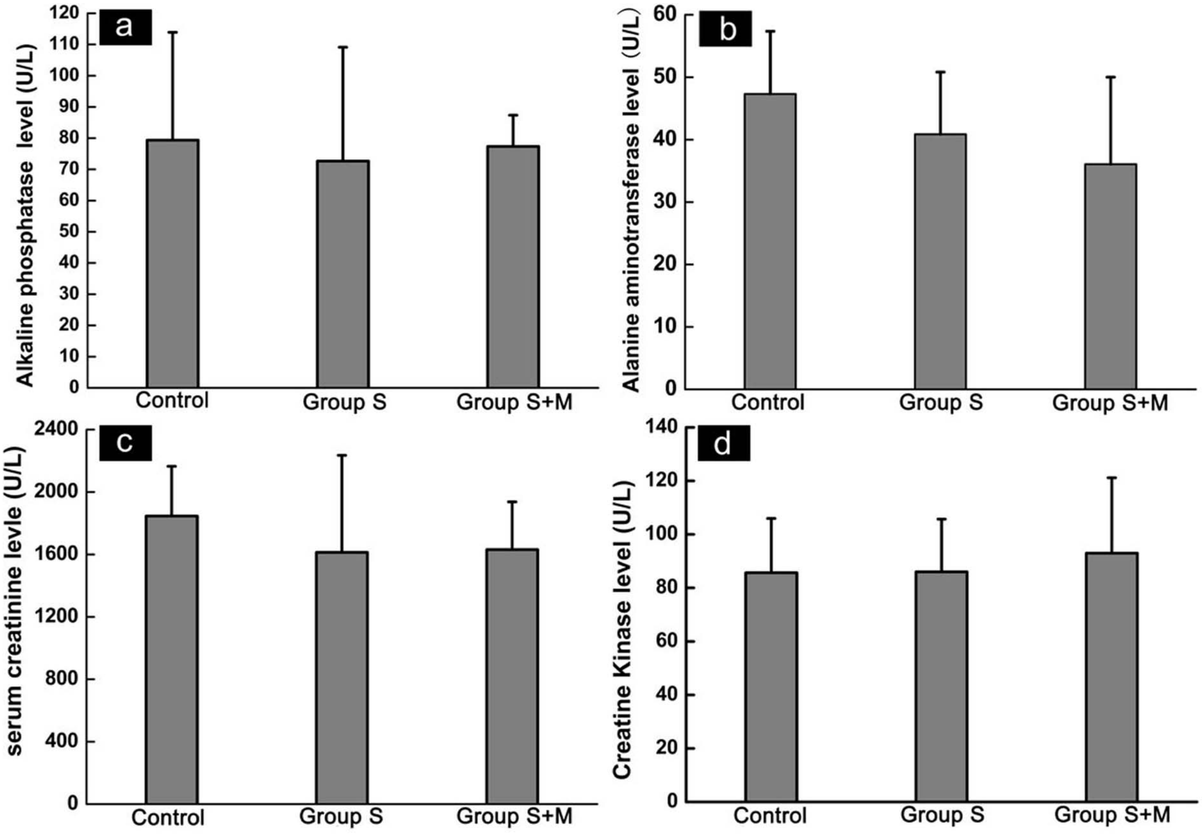

Figure 7 | **Serum ALP (a), ALT (b), Cr (c) and CK (d) post 30 day implantation of scaffolds.**

dimercaptosuccinic acid (MNP) was prepared according to a protocol described in our previous reference[39]. Hydroxyapatite nanoparticles (nHA) were purchased from Nanjing Emperor Nano Material Co., Ltd (purity: 97%, major diameter: 20 nm). Poly (DL-lactide) (PLA) with an average molecular weight of 10 kDa was purchased from Chengdu Dikang Biomedical Co., Ltd. Nanofibrous film was prepared according to the procedure in reference[35]. In brief, 2.5 g of MNP and 10 g of nHA were dispersed homogeneously in 10 mL of dimethylacetamide (DMAc by aid of a probe ultrasonication. Next, 20 g of PLA was dissolved in above suspension. The resulting mixture was electrospun to form nanofibrous nonwoven films. In order to fit bone defect shape in animal model, the films were folded carefully to fabricate pellets with the same volume and mass. The diameter of the pellets was about 0.5 cm. All samples were sterilized with ethylene oxide. The morphology of electrospun nanofibers was observed by scanning electron microscope (SEM, Hitch s-5200) and transmission electron microscope (TEM, JEOL JEM-1400), using conventional sample preparation methods.

Implantation surgery in rabbit model. The animal experiment protocol was approved by the Animal Care and Use Committee of Peking Union Medical College. All surgery was performed under sodium pentobarbital anesthesia, and all efforts were made to minimize suffering.

Three-month-old New Zealand white rabbits weighting 2.0–2.5 kg were used to create bone defect model. All animals were kept in the Animal center of the Institute of Basic Medical Sciences, Chinese Academy of Medical Sciences (Beijing, China) and randomly divided into 2 groups: (1) group S: scaffold group ($n = 12$); (2) group S + M: scaffold plus applied magnetic field group ($n = 12$). The animals were used in the following studies: a) biochemical analysis, H&E, perl's blue, oesteocalcin (OC) and sirius red staining ($n = 9$ for each group, three rabbits per time point: day 10, 20, and 30), b) CT analysis: the rabbits were continually scanned by CT at different time point ($n = 3$ for each group). c) microCT analysis: On day 110, the rabbits for CT scan analysis were scarified and the defects were analyzed through Micro-CT. Then the bone defects further underwent histological analysis.

Surgery procedure. The animals were anesthetized by a combination of phenobarbital sodium (30 $\mathrm{mg\ kg^{-1}}$ Merck, Germany) and procaine (5 $\mathrm{mg\ kg^{-1}}$). The surgical approach was median and posterior over the dosal spines of vertebrae L5 and L6, which were located by palpation and their distance from the iliac crests. The surgical site was shaved and scrubbed with iodine. Using sterile instruments and aseptic technique, a 2 cm dorsal median skin incision was made. The subcutaneous tissue, musculature periosteum was dissected and reflected to expose the transverse process of L5. Using a small rongeur, partial process was excised about 1 cm from the vertebral body, mimicking a partial laminectomy defect. The bone defects were filled with electrospun scaffold pellets. The wound was sutured layer by layer and no external fixation was applied.

Animal cages and animal care post the surgery. After surgery, rabbits in group S + M were raised in the cages with permanent magnets fixed on the opposite two sides of the cages (Figure S1), The magnets provided a static magnetic field in the cages, which was measured by Tesla meter (VSM, Lakeshore 7407). The intensity distribution of magnetic fields near the permanent magnets was showed in Figure S2. The magnetic intensity was 0.05–0.2 mT for the middle plane of the cage, and 5–25 mT for the two sides, as shown in Figure S3. Rabbits in group S were raised in the normal cages without magnets. All rabbits post surgery were given muscle injection of penicillin (Lu Kang Pharmace utical Co. Ltd., Shandong, China) with a dose of 400,000 units for 3 days.

CT examination and image analysis. New bone formation was evaluated by computer tomography measurements of each animal on day 10, 50 and day 90 post implantation of scaffolds. After being anesthetized by sodium pentobartital and maintained in prone position, animals were scanned with Dual Source CT scanner (Somatom Sensation 64, Siemens Medical Solutions, Forchheim, Germany) and the data were then reconstructed as three dimensional (3D) images using a MMWP working platform with 3D software (Siemens, Germany). The scan coverage was form xiphoid to the coccyx. The scanning parameters were as follows: 40 mAs; 120 KV; collimation 0.6 mm; FOV 20 cm; interval 0.6 mm. CT images were reconstructed with a thin slice thickness of 1 mm for diagnostic evaluation. All images were presented in a random order to two each experienced radiologists, who were blinded to the pathologic result and the model type of the animals.

Histological observation. The samples of transverse processes defects implanted with scaffolds were collected on the day 10, 20 and 30, and fixed with 10% neutral buffered formalin, and then transferred into 70% ethyl alcohol. Tissue samples for paraffin sections were decalcified with 10% ethylenediamine tetraacetic acid (EDTA) solution for 8 weeks, then dehydrated in a series of graded ethanol, and embedded in paraffin. Longitudinal sections cut at 5 μm were used for hematoxylin and eosin (H&E) staining. Transmitted light images of the stained sections were taken with Olympus BX53 microscope connected with a CCD camera (DP72; Olympus, Japan) allowing to record pictures with the Cellsense standard software (Olympus, Japan).

Iron staining. To directly visualize the scaffold-associated iron oxide particles, the sections previously prepared were stained with perl's reagent made of equal volumes of potassium ferrocyanide prepared in two-fold concentrated PBS and 2% hydrochloric acid in distilled water. The sections were immersed in the reagent for 20 minutes. After washing in distilled water, the sections were counterstained with neutral red for 5 minutes. Sections were dehydrated, covered for observation under an Olympus BX53 microscope. The iron parts became bright blue and the nuclei became red.

Collagen and osteocalcin staining. Sirius red dye is a strong anionic dye used for measuring collagen. The sections were deparaffinized and hydrated via a descending ethanol series followed by washing in running water. The specimens were stained with hematoxyl for 8 min and then immersed into in sirius red solution (0.1% in saturated picric acid, Sigma Aldrich) for 1 h. The sections were then washed in acidified water followed by dehydration and mounting. The stained sections were observed by a polarized microscope (BX53, Olympus, Japan).

For immunohistochemical staining of osteocalcin, the sections were deparaffinized, and then antigen retrieval was performed with a pressure cooker treatment by soaking the sections in a sodium citrate buffer for 10 min. After blocking endogenous peroxidase, the sections were incubated with goat serum at room temperature for 10 min to block nonspecific staining, and then with a primary mouse monoclonal antibody (1 : 100, Abcam Hong Kong Ltd) overnight at 4°C. Peroxidase activity was detected using enzyme substrate of diaminobenzidine (DAB). For negative controls, sections were treated in an identical manner with the exception that they were incubated in Tris-buffered saline without primary antibody.

Micro-CT and histological analysis at the terminal of healing. Processes with implantation were excised on day 110 and fixed in 4% of paraformaldeheyde for 24 h at 4°C. The specimens were wrapped in parafilm and scanned in air using a commercially available microCT scanner (SkyScan 1172, Bruker). After reconstruction, the volume of interest (VOI) was represented by an inner region of the reconstructed images of the scaffold implantation. In order to eliminate potential edge effects, the VOI was selected to be slightly smaller than the scaffold diameter to reduce interfacial errors. Thereafter, the samples were decalcified, dehydrated and embedded in paraffin for further staining with hematoxylin and eosin (H&E).

Biochemical analysis. To evaluate biocompatibility of the scaffolds, blood samples were collected from the rabbits at designated time points post surgery. Alkaline phosphatase (ALP), alanine aminotransferase (ALT), creatinine (Cr) and creatinine kinase (CK) in the serum were examined using automated chemistry analyzer (Olympus AU-5400, Japan).

Statistical analysis. Data are presented as the mean ± standard derivation. The statistical significance of the differences between the experimental groups was evaluated using a two tail Student's *t*-test for unpaired values. A value of $p < 0.1$ was considered statistically significant.

1. Kasoju, N. & Bora, U. Silk fibroin in tissue engineering. *Adv. Healthc. Mater.* **1**, 393–412 (2012).
2. Dinopoulos, H., Dimitriou, R. & Giannoudis, P. V. Bone graft substitutes: What are the options? *Surgeon.* **10**, 230–9 (2012).
3. Gloria, A., De Santis, R. & Ambrosio, L. Polymer-based composite scaffolds for tissue engineering. *J. Appl. Biomater. Biomech.* **8**, 57–67 (2010).
4. Wu, C., Chang, J. & Xiao, Y. Mesoporous bioactive glasses as drug delivery and bone tissue regeneration platforms. *Ther. Deliv.* **2**, 1189–98 (2011).
5. Bueno, E. M. & Glowacki, J. Cell-free and cell-based approaches for bone regeneration. *Nat. Rev. Rheumatol.* **5**, 685–97 (2009).
6. Robling, A. G., Burr, D. B. & Turner, C. H. Recovery periods restore mechanosensitivity to dynamically loaded bone. *J. Exp. Biol.* **204**, 3389–99 (2001).
7. Giannoudis, P. V., Einhorn, T. A. & Marsh, D. Fracture healing: the diamond concept. *Injury.* **38**, S3–6 (2007).
8. Hente, R., Fuchtmeier, B., Schlegel, U., Ernstberger, A. & Perren, S. M. The influence of cyclic compression and distraction on the healing of experimental tibial fractures. *J. Orthop. Res.* **22**, 709–715 (2004).
9. Zeichen, J., van Griensven, M. & Bosch, U. The proliferative response of isolated human tendon fibroblasts to cyclic biaxial mechanical strain. *Am. J. Sports. Med.* **28**, 888–892 (2000).
10. Kaspar, D., Seidl, W., Neidlinger-Wilke, C., Ignatius, A. & Claes, L. Dynamic cell stretching increases human osteoblast proliferation and CICP synthesis but decreases osteocalcin synthesis and alkaline phosphatase activity. *J. Biomech.* **33**, 45–51 (2000).
11. Jin, M., Frank, E. H., Quinn, T. M., Hunziker, E. B. & Grodzinsky, A. J. Tissue shear deformation stimulates proteoglycan and protein biosynthesis in bovine cartilage explants. *Arch. Biochem. Biophys.* **395**, 41–48 (2001).
12. Grace, K. L., Revell, W. J. & Brookes, M. The effects of pulsed electromagnetism on fresh fracture healing: osteochondral repair in the rat femoral groove. *Orthopedics.* **21**, 297–302 (1998).
13. Glazer, P. A., Heilmann, M. R., Lotz, J. C. & Bradford, D. S. Use of electromagnetic fields in a spinal fusion. A rabbit model. *Spine.* **22**, 2351–2356 (1997).
14. Takano-Yamamoto, T., Kawakami, M. & Sakuda, M. Effect of a pulsing electromagnetic field on demineralized bone-matrix-induced bone formation in a bony defect in the premaxilla of rats. *J. Dent. Res.* **71**, 1920–1925 (1992).
15. Miller, G. J., Burchardt, H., Enneking, W. F. & Tylkowski, C. M. Electromagnetic stimulation of canine bone grafts. *J. Bone Joint Surg. Am.* **66**, 693–698 (1984).

16. Bruce, G. K., Howlett, C. R. & Huckstep, R. L. Effect of a static magnetic field on fracture healing in a rabbit radius. Preliminary results. *Clin. Orthop. Relat. Res.* **222**, 300–306 (1987).
17. Yan, Q. C., Tomita, N. & Ikada, Y. Effects of static magnetic field on bone formation of rat femurs. *Med. Eng. Phys.* **20**, 397–402 (1998).
18. Assiotis, A., Sachinis, N. P. & Chalidis, B. E. Pulsed electromagnetic fields for the treatment of tibial delayed unions and nonunions. A prospective clinical study and review of the literature. *J. Orthop. Surg. Res.* **7**, 24 (2012).
19. Chalidis, B., Sachinis, N., Assiotis, A. & Maccauro, G. Stimulation of bone formation and fracture healing with pulsed electromagnetic fields: biologic responses and clinical implications. *Int. J. Immunopathol. Pharmacol.* **24**, 17–20 (2011).
20. Jaberi, F. M. *et al.* moderate-intensity static magnetic field enhances repair of cartilage damage in rabbits. *Arch. Med. Res.* **42**, 268–273 (2011).
21. Torbet, J. & Ronziere, M. C. Magnetic alignment of collagen during self-assembly. *Biochem. J.* **219**, 1057–1059 (1984).
22. Murthy, N. S. Liquid crystallinity in collagen solutions and magnetic orientation of collagen fibrils. *Biopolymers.* **23**, 1261–1267 (1984).
23. Torbet, J., Freyssinet, J. M. & Hudry-Clergeon, G. Oriented fibrin gels formed by polymerization in strong magnetic fields. *Nature.* **289**, 91–93 (1981).
24. Ueno, S., Iwasaka, M. & Tsuda, H. Effects of Magnetic-Fields on Fibrin Polymerization and Fibrinolysis. *IEEE. TRANS. MAGN.* **29**, 3352–3354 (1993).
25. Iwasaka, M., Ueno, S. & Tsuda, H. Effects of Magnetic-Fields on Fibrinolysis. *J. Appl. Phys.* **75**, 7162–7164 (1994).
26. Yamagishi, A., Takeuchi, T., Higashi, T. & Date, M. Diamagnetic Orientation of Blood-Cells in High Magnetic-Field. *Physica B.* **177**, 523–526 (1992).
27. Higashi, T. *et al.* Orientation of erythrocytes in a strong static magnetic field. *Blood.* **82**, 1328–1334 (1993).
28. Higashi, T., Yamagishi, A., Takeuchi, T. & Date, M. Effects of Static Magnetic-Fields on Erythrocyte Rheology. *Bioelectrochem. Bioenerg.* **36**, 101–108 (1995).
29. Higashi, T., Sagawa, S., Kawaguchi, N. & Yamagishi, A. Effects of a strong static magnetic field on blood platelets. *Platelets.* **4**, 341–342 (1993).
30. Vassilev, P. M., Dronzine, R. T., Vassileva, M. P. & Georgiev, G. A. Parallel arrays of microtubules formed in electric and magnetic fields. *Biosci. Rep.* **2**, 1025–1029 (1982).
31. Kotani, H. *et al.* Strong static magnetic field stimulates bone formation to a definite orientation in vitro and in vivo. *J. Bone. Miner. Res.* **17**, 1814–1821 (2002).
32. Leesungbok, R. *et al.* The effects of a static magnetic field on bone formation around a SLA treated titanium implant. *J. Oral. Implantol.* **39**, 248–255 (2013).
33. Serantes, D., Baldomir, D. & Pereiro, M. Nonmonotonic evolution of the blocking temperature in dispersions of superparamagnetic nanoparticles. *Phys. Rev. B: Condens. Mater.* **82**, 134433 (2010).
34. De Santis, R. *et al.* A basic approach toward the development of nanocomposite magnetic scaffolds for advanced bone tissue engineering. *J. Appl. Polym. Sci.* **12**, 3599–3605 (2011).
35. Meng, J. *et al.* Paramagnetic nanofibrous composite films enhance the osteogenic responses of pre-osteoblast cells. *Nanoscale.* **2**, 2565–2569 (2010).
36. Zeng, X. B. *et al.* Magnetic responsive hydroxyapatite composite scaffolds construction for bone defect reparation. *Int. J. Nanomedicine.* **7**, 3365–3378 (2012).
37. Panseri, S. *et al.* Magnetic hydroxyapatite bone substitutes to enhance tissue regeneration: evaluation in vitro using osteoblast-like cells and in vivo in a bone defect. *PLoS One.* **7**, e38710 (2012).
38. Gloria, A. *et al.* Magnetic poly(ε-caprolactone)/iron-doped hydroxyapatite nanocomposite substrates for advanced bone tissue engineering. *J. R. Soc. Interface.* **10**, 20120833 (2013).
39. Liu, J. W. *et al.* Synthesis, Characterization, and Application of Composite Alginate Microspheres with Magnetic and Fluorescent Functionalities. *J. Appl. Polym. Sci.* **113**, 4042–4051 (2009).
40. Liu, W., Thomopoulos, S. & Xia, Y. Electrospun nanofibers for regenerative medicine. *Adv. Healthc. Mater.* **1**, 10–25 (2012).
41. Venugopal, J. *et al.* Biomimetic hydroxyapatite-containing composite nanofibrous substrates for bone tissue engineering. *Philos. Transact. A. Math. Phys. Eng. Sci.* **368**, 2065–81 (2010).
42. Zhang, Z., Hu, J. & Ma, P. X. Nanofiber-based delivery of bioactive agents and stem cells to bone sites. *Adv. Drug. Deliv. Rev.* **64**, 1129–41 (2012).
43. Prabhakaran, M. P., Ghasemi-Mobarakeh, L. & Ramakrishna, S. Electrospun composite nanofibers for tissue regeneration. *J. Nanosci. Nanotechnol.* **11**, 3039–57 (2011).
44. Holzwarth, J. M. & Ma, P. X. Biomimetic nanofibrous scaffolds for bone tissue engineering. *Biomaterials.* **32**, 9622–9 (2011).
45. Yuge, L. *et al.* Physical stress by magnetic force accelerates differentiation of human osteoblasts. *Biochem. Biophys. Res. Commun.* **311**, 32–8 (2003).

Acknowledgements

Authors thank for financial support from National Key Program of China (2011CB933500) and Beijing Municipal Natural Science Foundation (2102046). Authors thank Dr Xiao Chang and Dr Yanyan Bian for their precious help in the animal surgery of implantation.

Author contributions

H.X. and N.G. designed experiments, made data analysis and wrote the main manuscript. J.M. and B.X. prepared scaffolds, conducted animal experiments and made data analysis; prepared all figures and discussed all sections of the manuscript with the corresponding authors. Y.Z. and J.L. prepared super-paramagnetic nanoparticles, measured magnetic field strength, and prepared supporting information. H.X., J.L. and Z.J. conducted CT and microCT imaging and made data analysis. H.K. prepared electrospun films and made morphological characterization. Y.H. instructed animal surgery. All authors reviewed the manuscript.

Additional information

Supplementary information accompanies this paper at http://www.nature.com/scientificreports

Competing financial interests: The authors declare no competing financial interests.

How to cite this article: Meng, J. *et al.* Super-paramagnetic responsive nanofibrous scaffolds under static magnetic field enhance osteogenesis for bone repair *in vivo*. *Sci. Rep.* **3**, 2655; DOI:10.1038/srep02655 (2013).